



A sparsity-based iterative algorithm for reconstruction of micro-CT images from highly undersampled projection datasets obtained with a synchrotron X-ray source

S. Ali Melli, Khan A. Wahid, Paul Babyn, David M. L. Cooper, and Varun P. Gopi

Citation: *Review of Scientific Instruments* **87**, 123701 (2016); doi: 10.1063/1.4968198

View online: <http://dx.doi.org/10.1063/1.4968198>

View Table of Contents: <http://scitation.aip.org/content/aip/journal/rsi/87/12?ver=pdfcov>

Published by the AIP Publishing

Articles you may be interested in

Computational and human observer image quality evaluation of low dose, knowledge-based CT iterative reconstruction

Med. Phys. **42**, 6098 (2015); 10.1111/1.4929973

Combined iterative reconstruction and image-domain decomposition for dual energy CT using total-variation regularization

Med. Phys. **41**, 051909 (2014); 10.1111/1.4870375

Characterization of adaptive statistical iterative reconstruction algorithm for dose reduction in CT: A pediatric oncology perspective

Med. Phys. **39**, 5520 (2012); 10.1111/1.4745563

Algorithms for sparse X-ray CT image reconstruction of objects with known contour

AIP Conf. Proc. **1430**, 597 (2012); 10.1063/1.4716282

Sparseness prior based iterative image reconstruction for retrospectively gated cardiac micro-CT

Med. Phys. **34**, 4476 (2007); 10.1111/1.2795830



Nanopositioning Systems

Micropositioning

AFM & SPM

Single molecule imaging

A sparsity-based iterative algorithm for reconstruction of micro-CT images from highly undersampled projection datasets obtained with a synchrotron X-ray source

S. Ali Melli,^{1,a)} Khan A. Wahid,¹ Paul Babyn,² David M. L. Cooper,³ and Varun P. Gopi⁴

¹Department of Electrical and Computer Engineering, University of Saskatchewan, Saskatoon, Saskatchewan S7N5A9, Canada

²Department of Medical Imaging, Royal University Hospital, University of Saskatchewan, Saskatoon, Saskatchewan S7N 0W8, Canada

³Department of Anatomy and Cell Biology, College of Medicine, University of Saskatchewan, Saskatoon, Saskatchewan S7N 5E5, Canada

⁴Department of Electronics and Communication Engineering, Government Engineering College Wayanad, Mananthavady, India

(Received 16 June 2016; accepted 8 November 2016; published online 8 December 2016)

Synchrotron X-ray Micro Computed Tomography (Micro-CT) is an imaging technique which is increasingly used for non-invasive *in vivo* preclinical imaging. However, it often requires a large number of projections from many different angles to reconstruct high-quality images leading to significantly high radiation doses and long scan times. To utilize this imaging technique further for *in vivo* imaging, we need to design reconstruction algorithms that reduce the radiation dose and scan time without reduction of reconstructed image quality. This research is focused on using a combination of gradient-based Douglas-Rachford splitting and discrete wavelet packet shrinkage image denoising methods to design an algorithm for reconstruction of large-scale reduced-view synchrotron Micro-CT images with acceptable quality metrics. These quality metrics are computed by comparing the reconstructed images with a high-dose reference image reconstructed from 1800 equally spaced projections spanning 180°. Visual and quantitative-based performance assessment of a synthetic head phantom and a femoral cortical bone sample imaged in the biomedical imaging and therapy bending magnet beamline at the Canadian Light Source demonstrates that the proposed algorithm is superior to the existing reconstruction algorithms. Using the proposed reconstruction algorithm to reduce the number of projections in synchrotron Micro-CT is an effective way to reduce the overall radiation dose and scan time which improves *in vivo* imaging protocols. Published by AIP Publishing. [<http://dx.doi.org/10.1063/1.4968198>]

I. INTRODUCTION

X-ray Computed Tomography (CT) is a non-invasive imaging technique where projections (radiographs) taken from different viewing angles are processed by a computer to reconstruct the cross-sectional (tomographic) image of the scanned object. After the development of the digital computer, the first commercial CT scanner was introduced early in the 1970s.¹ Since then, there have been competing trends to increase scanner resolution and decrease the needed X-ray dose. Micro Computed Tomography (Micro-CT) scanners can provide high spatial resolution.² Micro-CT using synchrotron X-ray radiation sources can provide a spatial resolution between 1 and 10 μm.³ Synchrotron beamlines generate parallel beam monochromatic X-rays in a pre-selectable energy to eliminate cone beam and beam-hardening artifacts. Synchrotron X-rays are also highly intense which boosts the signal to noise ratio allowing faster scan time.^{4,5} Thus, these advantages of synchrotron Micro-CT make this imaging method an important tool for biological research and an excellent platform for

testing reconstruction algorithm improvements which can be ported to conventional systems.

Traditionally, tomographic reconstruction techniques require a large number of projection views to reconstruct synchrotron micro tomographic images with the fine spatial resolution necessary to view as much detail as possible in the sample field of view.⁶ This exposes the specimen to a large amount of X-ray radiation which can damage living specimens. This also increases scan time and consequently the likelihood of involuntary specimen movements so motion artifact in the reconstructed images will be more likely. One way to reduce the overall scan time and radiation dose is to reduce the acquisition time for each projection; in fact, this is the only parameter that can be used to control the amount of synchrotron radiation at each angle as the radiation intensity is almost constant per projection.⁷ However, detector sensitivity and readout speed may not allow the exposure time per projection to be less than a certain value. Also, a very noisy tomographic image will be reconstructed in a low exposure time per projection because of the low projection signal to noise ratio.⁸ Another approach for decreasing the total scan time and radiation dose is to reduce the number of projections needed to reconstruct the tomographic images. Analytical reconstruction methods such as Filtered Back

^{a)}Author to whom correspondence should be addressed. Electronic mail: sem649@mail.usask.ca. Telephone: 306-203-3988. Fax: 306-966-5407.

Projection (FBP) which are often used in medical CT scanners have acceptable performance when there are a large number of closely sampled projections over the scanning angular range, otherwise, aliasing artifacts will occur in the reconstructed image.⁹ On the other hand, iterative reconstruction methods such as Projection onto Convex Sets (POCSs)^{10,11} can be utilized to reconstruct high-quality tomographic images when noisy and/or slightly reduced projection data are available. Methods based on iteratively solving linear tomographic equations may also fail to maintain image quality with a highly reduced number of projections. The reason is that when the number of projections is severely reduced, the linear tomographic equations will be highly ill-conditioned, and the subsequently reconstructed image will be highly sensitive to data noise and modeling error.¹²

Lately, Compressed Sensing (CS) theory has spurred great interest in the signal-processing research community. Although there are no equations that show the relationship between image sparsity and sufficient number of projections for tomographic image recovery in CS theory, the results in Refs. 13 and 14 demonstrate that a phase transition from non-recovery to recovery as happened in compressed sensing can also take place in sparse-view tomographic reconstruction. For practical large-scale tomographic reconstruction, a compressed sensing algorithm called ASD-POCS was proposed in Refs. 15 and 16 to minimize the total variation (TV) of the image subject to the constraint that the estimated projection data are within a specified tolerance of the available data and that the values of the volume image are non-negative. In Ref. 17, the application of this algorithm to low-dose Micro-CT of real animal organs was investigated. The problem of this heuristic algorithm is that the reconstructed image depends on the parameters of the optimization problem, which the algorithm aims to solve, and all the parameters of the algorithm itself.¹⁸ More parameters make characterization of the algorithm more difficult. Moreover, the nonsmooth regularizers such as sparsity-promoting ones based on the l_1 -norm are not differentiable everywhere, so conventional methods (e.g., ASD-POCS) employ differentiable approximation (e.g., using “corner-rounding”) which leads to slow convergence.¹⁹ For solving this problem, in the past few years, state-of-the-arts first-order splitting based algorithms such as (M)FISTA,^{20,21} Split-Bregman-type (SB),²² ADMM,²³ and Chambolle-Pock^{24,25} which can handle nonsmooth regularizers without corner rounding were proposed. These algorithms are inter-related,²⁶ but there are differences in parameterization which can have a significant impact on the convergence in practice. The Split-Bregman (SB) method converges to a reasonable practically useful precision quickly and was used in the reduced-view CT reconstruction algorithm (SpBR-TV).²⁷ However, total variation (TV)-based reconstruction algorithms such as SpBR-TV have been shown to work well when dealing with piecewise smooth images, but it may lead to unwanted staircase artifact when applied to images that contain textures and shading.^{28,29}

Our proposed algorithm combines gradient-based Douglas-Rachford Splitting (DRS) and discrete wavelet packet shrinkage image denoising methods to design an algorithm for the reconstruction of large-scale synchrotron

Micro-CT images from a reduced number of projections. The DRS method is a simple but powerful method for distributed convex programming first proposed in Ref. 30 for solutions of small-scale and easy-to-solve sub-problems which can be coordinated to find the solution of large-scale optimization problems. This method was used to solve the gradient-based large scale compressed sensing optimization problem to reconstruct uniform regions within organs while preserving strong edges at organ boundaries. The discrete wavelet packet shrinkage image denoising was used to mitigate the effect of any potential noise in the final reconstructed image.³¹ The wavelet packet transform compacts the energy of prominent features (e.g., edges) which are dominant and global into a small number of coefficients with large magnitude, and spreads the energy of noise which is sub-dominant and local into a large number of coefficients with small magnitude. Typically, keeping large coefficients and removing small ones reduces the energy of the noise.^{32,33}

II. MATERIAL AND METHODS

A. Synchrotron Micro-CT data acquisition

Micro-CT data were obtained from at the Biomedical Imaging and Therapy Bending Magnet (BMIT-BM) beamline at the Canadian Light Source (CLS). This is a bend magnet beamline with a field strength of 1.354 T. The ring energy is 2.9 GeV and the storage ring current is a maximum of 250 mA operating in decay mode. The critical energy of the bend magnet source is 7.57 keV. The beamline uses a Si (2,2,0) Bragg double crystal monochromator at a distance of 13.2 m from the source. A block of femoral cortical bone was placed on a rotating mechanical stage that was 26 m away from the synchrotron source so that the X-ray beam can be assumed to be parallel. Projection data were collected with a Hamamatsu C9300 (Hamamatsu Photonics, Hamamatsu, Japan) CCD camera fitted with a beam monitor with a 10 μm thick gadolinium oxysulfide scintillator. The white beam filtered with aluminum (6 mm) and tin (0.5 mm) was used to generate a spike of X-rays in the 25–29 keV energy range. The sample was rotated through 180° in 0.1° steps, generating 1800 projections. An exposure time of 1 s/frame and two-frame averaging was employed for each of the 1800 projections. The optical configuration provided an effective pixel size of 5 μm . Dark and flat projections were taken before and after the sequential angular projections. The acquisition system used 12 bit TIFF greyscale digital format to save the calibration and tomographic data.

B. Synchrotron Micro-CT data preprocessing

Projection data required preprocessing before sinogram formation, including dark and flat field correction, projection alignment, beam power normalization, and logarithm transformation. Dark and flat field correction compensates spatial variation in beam intensity caused by different detector pixel sensitivities and/or distortions in optical path and it also compensates different dark currents in detector pixels so that a

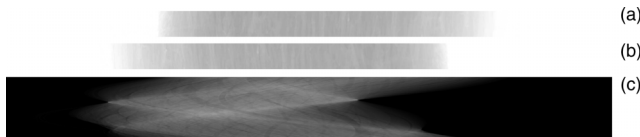


FIG. 1. (a) Projection dataset at angle 0°, (b) projection dataset at angle 180°, (c) sinogram dataset (270 views).

uniform signal creates a uniform output. Projection alignment was needed because it is practically difficult to exactly match specimen rotation center with the center of the projection images and finally beam power normalization was used to compensate the slight variations in the beam intensity happening over time. After logarithm transformation, the full sinogram dataset (1800 projections) was formed by collecting the preprocessed signal along a specific detector row in the 2D projection plane for all angular views along the 180° angular range and arranging them side by side to reconstruct the reference image. Also, the projection data were sampled uniformly along angular views and preprocessed to produce undersampled sinogram datasets which were used in the reconstruction algorithms. Ring artifacts created by defective pixels on the detector or a small variation in filtered beam can be removed from full and undersampled sinogram datasets before the application of the reconstruction algorithms.³⁴ 121 by 2791 pixel preprocessed projection datasets which were acquired at angles 0° and 180° (initial and final angles) and a 270 by 2791 pixel sinogram dataset which was created by putting together the middle rows of the preprocessed projection data of 270 angular views along the 180° angular range were shown in Fig. 1.

C. Imaging model and optimization formulation

The basic algebraic imaging model for a 2D synchrotron X-ray Micro-CT is

$$y = Au, \quad (1)$$

where $u \in R^n$ is a vector of image pixel values modeling spatially varying linear attenuation coefficient and $A \in R^{m \times n}$ is the discrete Radon transform¹¹ modeling the parallel forward projection operator which yields noisy undersampled ($m < n$) sinogram dataset $y \in R^m$. As discussed in Refs. 35–37 and 39, both sides of Eq. (1) can be multiplied by the FBP operator to form an equivalent preconditioned Equation (2). The eigenvalues of square matrix FA which is diagonally dominant with positive diagonal elements are positive and clustered closer together than the eigenvalues of square matrix $A^T A$,³⁷

$$Fy = FAu, \quad F = A^T R. \quad (2)$$

The superscript T represents the transpose operation, A^T is the discrete counterpart of the adjoint of the Radon transform modeling the parallel back-projection operator, and R is the discrete counterpart of 1D convolution operator (band-limited ramp filter kernel) which is defined in the discrete inverse Radon transform.³⁸ To view this as an optimization problem, we must find a generalized squared-error function that is minimized by the solution u given by Eq. (2),³⁹

$$f_1(u) \equiv \frac{1}{2} \|Au - y\|_R^2 = \frac{1}{2}(Au - y)^T R(Au - y). \quad (3)$$

It is clear that taking the derivative of Eq. (3) with respect to u and putting it equal to zero yields Eq. (2). On the other hand, the medical tomographic images are almost uniform within the organs with a small number of abrupt variations at the organ boundaries,¹⁸ so the 2D gradient transform is used as the sparsifying transformation.

According to the CS theory, an optimization problem called generalized Lasso^{40,41} is formed to search a sparse gradient image while minimizing the generalized squared-error function (3),

$$\min_{u \in R^n} \frac{1}{2} \|Au - y\|_R^2 + \lambda \|Gu\|_{l_1} \quad \lambda > 0, \quad (4)$$

where $G \in R^{2n \times n}$ is the 2D gradient operator defined in Eq. (5), $\|x\|_{l_1}$ is the ℓ_1 -norm which is defined as the sum of the absolute pixel values, and λ is the parameter which controls the trade-off between spatial resolution and the suppression of artifacts/noise,

$$\begin{aligned} Gh_{ij}(u) &:= \begin{cases} u_{i+1,j} - u_{i,j} & i < \sqrt{n} \\ 0 & i = \sqrt{n} \end{cases}, \\ Gv_{ij}(u) &:= \begin{cases} u_{i,j+1} - u_{i,j} & j < \sqrt{n} \\ 0 & j = \sqrt{n} \end{cases}, \\ G(u) &:= \begin{pmatrix} Gh_{ij}(u) \\ Gv_{ij}(u) \end{pmatrix}. \end{aligned} \quad (5)$$

D. Proposed reconstruction algorithm

Consider a generalization of problem (4) where a regularizing function is added to a data fidelity function, i.e.,

$$\min_{u \in R^n} f_1(u) + f_2(Gu), \quad (6)$$

where $f_1 : R^n \rightarrow R$ is a data fidelity function and $f_2 : R^p \rightarrow R$ is a regularizing function which is a closed, proper, and convex function and $G \in R^{p \times n}$ is an arbitrary linear operator.

Our approach to solve the optimization problem (6) is to convert it into an equivalent constrained optimization problem by using variable splitting method as shown in Eq. (7),

$$\min_{u, v} f_1(u) + f_2(v) \quad S.T. \quad v = Gu. \quad (7)$$

The global minima of a convex function subject to equality constraint can be found by forming an unconstrained optimization problem followed by a dual variable update as follows:⁴²

Loop

$$\min_{u, v} f_1(u) + f_2(v) + b^T(Gu - v) + \frac{1}{2\mu} \|Gu - v\|_{l_2}^2, \quad (8)$$

$$b := b + \frac{1}{\mu}(Gu - v), \quad (9)$$

Until stop condition is satisfied

where $b \in R^p$ is the vector of dual variables, $\|x\|_{l_2}$ is the Euclidean norm which is defined as the square root of the sum of the squared pixel values, and $\mu > 0$ is called the penalty parameter. The advantage of adding the penalty term

$\frac{1}{2\mu} \|Gu - v\|_{l_2}^2$ to the unconstrained formula is to guarantee the global algorithm convergence.

The optimization problem (8) and dual variables update formula (9) are rewritten in a new form by merging the linear function $b^T(Gu - v)$ and quadratic function $\frac{1}{2\mu} \|Gu - v\|_{l_2}^2$, and also scaling the dual variables

Loop

$$\min_{u,v} f_1(u) + f_2(v) + \frac{1}{2\mu} \|Gu - v + d\|_{l_2}^2 \quad d = \mu b, \quad (10)$$

$$d := d + (Gu - v). \quad (11)$$

Until stop condition is satisfied

The optimization problem in Eq. (10) is solved by applying the Douglas-Rachford Splitting (DRS) algorithm. This algorithm is helpful when the optimization problem with respect to u and v (Eqs. (12) and (13)) is efficiently solved while the joint minimization of Eq. (10) is difficult to evaluate. For that reason, Eq. (10) is decomposed into sub-optimization problems by separately minimizing with respect to u and v . These operations are followed by a dual variable update formula as below

Loop

$$u_{k+1} := \min_u f_1(u) + \frac{1}{2\mu} \|Gu - (v_k - d_k)\|_{l_2}^2, \quad (12)$$

$$v_{k+1} := \min_v f_2(v) + \frac{1}{2\mu} \|v - (Gu_{k+1} + d_k)\|_{l_2}^2, \quad (13)$$

$$d_{k+1} := d_k + (Gu_{k+1} - v_{k+1}), \quad (14)$$

Until stop condition is satisfied

where k is a loop counter. The convergence analysis of the DRS algorithm was discussed in Ref. 43. It shows that it is not necessary to exactly solve the minimization problem in Eqs. (12) and (13); provided that sequence of errors is absolutely summable, global convergence will be guaranteed. Depending on the functions used in Eqs. (12) and (13), closed form or iterative formulations are used to update u and v efficiently. If the data fidelity function $f_1(u)$ is smooth, which is normally the case, the gradient method can be used to solve Eq. (12). Moreover, the regularizing function $f_2(v)$ which is normally used in the compressed sensing reconstruction is a non-smooth ℓ_1 -norm function. In this case, sub differential calculus and proximal operator⁴⁴ defined in Eq. (15) can be used to evaluate Eq. (13). The proximal operator $\text{prox}_f : R^n \rightarrow R^n$ of f with parameter μ is defined by

$$\text{prox}_{\mu f}(w) := \min_s f(s) + \frac{1}{2\mu} \|s - w\|_{l_2}^2. \quad (15)$$

Using this operator and also smoothness of data fidelity function, the DRS algorithm equations are recast as follows:

Loop

$$u_{k+1} := \text{Root} \left(\frac{\partial f_1}{\partial u} + \frac{1}{\mu} G^T(Gu - (v_k - d_k)) \right), \quad (16)$$

$$v_{k+1} := \text{prox}_{\mu f_2}(Gu_{k+1} + d_k), \quad (17)$$

$$d_{k+1} := d_k + (Gu_{k+1} - v_{k+1}). \quad (18)$$

Until stop condition is satisfied

The described algorithmic framework is applied to Eq. (4). This problem has the form (6) with

$$f_1(u) \equiv \frac{1}{2} \|Au - y\|_R^2 = \frac{1}{2} (Au - y)^T R (Au - y), \quad (19)$$

$$f_2(v) \equiv \lambda \|v\|_{l_1}.$$

Derivative of quadratic data fidelity function $f_1(u)$ is $\frac{\partial f_1}{\partial u} = A^T R (Au - y)$ which is used to instantiate Eq. (16). After doing some basic mathematical operations, Eq. (20) is derived

$$u_{k+1} := (A^T R A + \frac{1}{\mu} G^T G)^{-1} (A^T R y + \frac{1}{\mu} G^T (v_k - d_k)). \quad (20)$$

The linear conjugate gradient (CG) method⁴⁵ is used to approximately solve this equation. The advantage of this method is that it can solve large-scale linear equations without a need to explicitly inverse the coefficient matrix.

Definition of the proximal operator, element-wise sub differential calculus, and derivative of absolute value⁴⁶ are used to instantiate Eq. (17). After doing some basic mathematical operations, Eq. (21) is derived

$$v_{k+1} := ST_{\mu,\lambda}(Gu_{k+1} + d_k), ST_\kappa(a) = \begin{cases} a - \kappa & a > \kappa \\ 0 & |a| \leq \kappa \\ a + \kappa & a < -\kappa \end{cases}. \quad (21)$$

This shrinkage operator which is called *soft threshold* operator is extremely fast and requires only a few operations per element of operand.

Additionally, the discrete wavelet packet shrinkage image denoising technique was used to suppress the remaining noise. Therefore, the Symlet⁴ 4-tap orthonormal wavelet filter bank, universal threshold selection rule,⁴⁷ and soft thresholding method were selected to be used in a 5-level wavelet packet decomposition and reconstruction.

Finally, the proposed algorithm is summarized as follows:

Initialize $\lambda > 0, \mu > 0, u = 0, v = 0, d = 0, k = 0$

Loop($k := k + 1$),

$$u_{k+1} := (A^T R A + \frac{1}{\mu} G^T G)^{-1} (A^T R y + \frac{1}{\mu} G^T (v_k - d_k)), \quad (22)$$

$$v_{k+1} := ST_{\mu,\lambda}(Gu_{k+1} + d_k), \quad (23)$$

$$d_{k+1} := d_k + (Gu_{k+1} - v_{k+1}), \quad (24)$$

$$\text{Until } \frac{\|u_{k+1} - u_k\|_{l_2}}{\|u_k\|_{l_2}} < \varepsilon,$$

$$u := WP^{-1}\Gamma_G WP(u), \quad (25)$$

where the operators WP and WP^{-1} stand for the forward and inverse discrete wavelet packet transformations, respectively, and Γ_G is a wavelet-domain point-wise threshold operator with a global threshold.

To decrease the convergence time, the linear conjugate gradient method should be initialized by solution u_k obtained in the previous DRS iteration. With this initialization procedure, the number of iterations in the CG method (inner iterations) reduces to a few numbers while the global DRS method (outer iterations) converges.⁴⁸

TABLE I. Quality metrics of reconstructed synthetic FORBILD head phantom images.

| Number of projections method | 15 | | | 25 | | | 45 | | | 90 | | |
|------------------------------|-------|--------|-------|-------|--------|-------|-------|--------|-------|-------|--------|-------|
| | SSIM | RE (%) | PSNR |
| Proposed | 0.773 | 21.78 | 26.31 | 0.986 | 8.64 | 33.58 | 0.995 | 3.82 | 38.96 | 0.996 | 2.93 | 40.09 |
| SpBR-TV | 0.664 | 32.88 | 24.35 | 0.897 | 13.11 | 29.77 | 0.923 | 8.96 | 31.57 | 0.995 | 3.28 | 39.12 |
| FBP | 0.187 | 69.93 | 16.18 | 0.223 | 48.80 | 18.36 | 0.294 | 29.69 | 21.17 | 0.472 | 19.45 | 23.66 |
| POCS | 0.400 | 44.26 | 20.15 | 0.448 | 36.94 | 20.78 | 0.496 | 27.51 | 21.85 | 0.622 | 19.98 | 23.43 |
| ASD-POCS | 0.557 | 35.78 | 22.00 | 0.780 | 22.85 | 24.95 | 0.911 | 18.16 | 25.44 | 0.959 | 12.26 | 27.67 |

E. Assessment of image quality

Both reference-based quantitative and visual assessments were used to compare the performance of the proposed algorithm with the other existing reconstruction methods. It is assumed that a high X-ray dose image is available to be used as a reference image against which the reconstructed image is to be compared.

1. Quantitative assessment

Structural SIMilarity (SSIM) index is a metric for measuring the structural similarity between two images. If ρ and t are two local image windows selected from the same position of two input images, SSIM is defined as follows:⁴⁹

$$SSIM(\rho, t) = \frac{2\mu_\rho\mu_t + C1}{\mu_\rho^2 + \mu_t^2 + C1} \cdot \frac{2\sigma_\rho\sigma_t + C2}{\sigma_\rho^2 + \sigma_t^2 + C2} \cdot \frac{\sigma_{\rho t} + C3}{\sigma_\rho\sigma_t + C3}, \quad (26)$$

where μ_ρ and μ_t are the averages, σ_ρ and σ_t are the standard deviations, and $\sigma_{\rho t}$ is the covariance of the local windows. $2C3 = C2$ and $C1$ are constants to stabilize division. The overall SSIM index is calculated by averaging the SSIM map along the entire image. A higher SSIM index indicates superior image quality.

Peak Signal to Noise Ratio (PSNR) and Relative error (RE) are error sensitive quality metrics defined as follows:

$$PSNR(db) = 10\log_{10}\left(\frac{Peak^2}{MSE}\right), \quad (27)$$

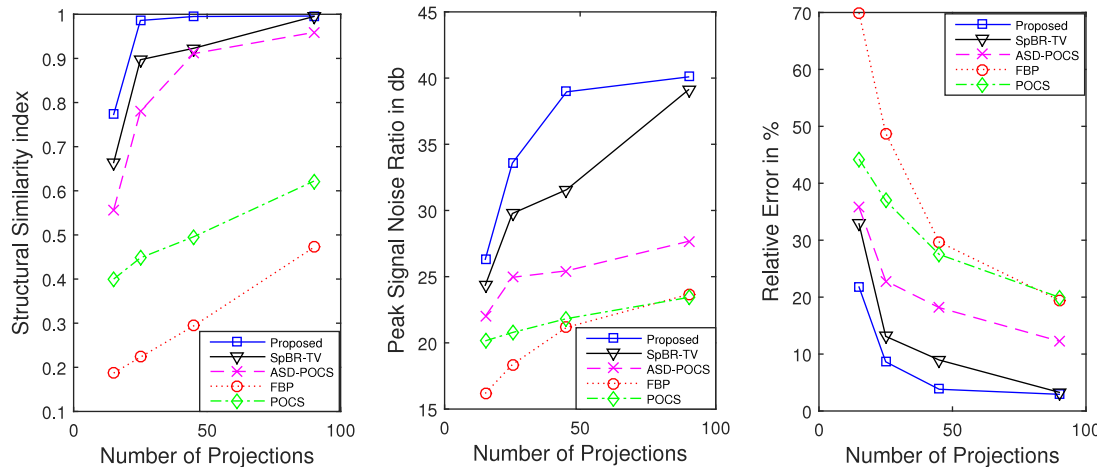


FIG. 2. Synthetic FORBILD head phantom image quality metrics vs number of projections.

where *Peak* is the highest pixel value, e.g., in the case of 12-bit pixel representation, it is 1023; MSE is the mean square error between the reconstructed and reference images,

$$RE(%) = \frac{\|u_{ref} - u_{rec}\|_2}{\|u_{ref}\|_2} \times 100, \quad (28)$$

where u_{rec} and u_{ref} are the reconstructed and reference images which are converted into the column vectors.

The SSIM index considers image degradations as perceived changes in structural information. Therefore, the SSIM index is more consistent than PSNR and RE with human visual system because human visual perception is highly adapted for extracting structural information from a scene.⁴⁹

2. Visual assessment

The images which were reconstructed by the different reconstruction algorithms, i.e., FBP, POCS, ASD-POCS, SpBR-TV, and the proposed algorithm at different numbers of projections were visually compared with the reference image to assess the reconstruction process.

III. EXPERIMENTAL RESULT AND DISCUSSION

The proposed algorithm along with four existing reconstruction methods was used to reconstruct a synthetic

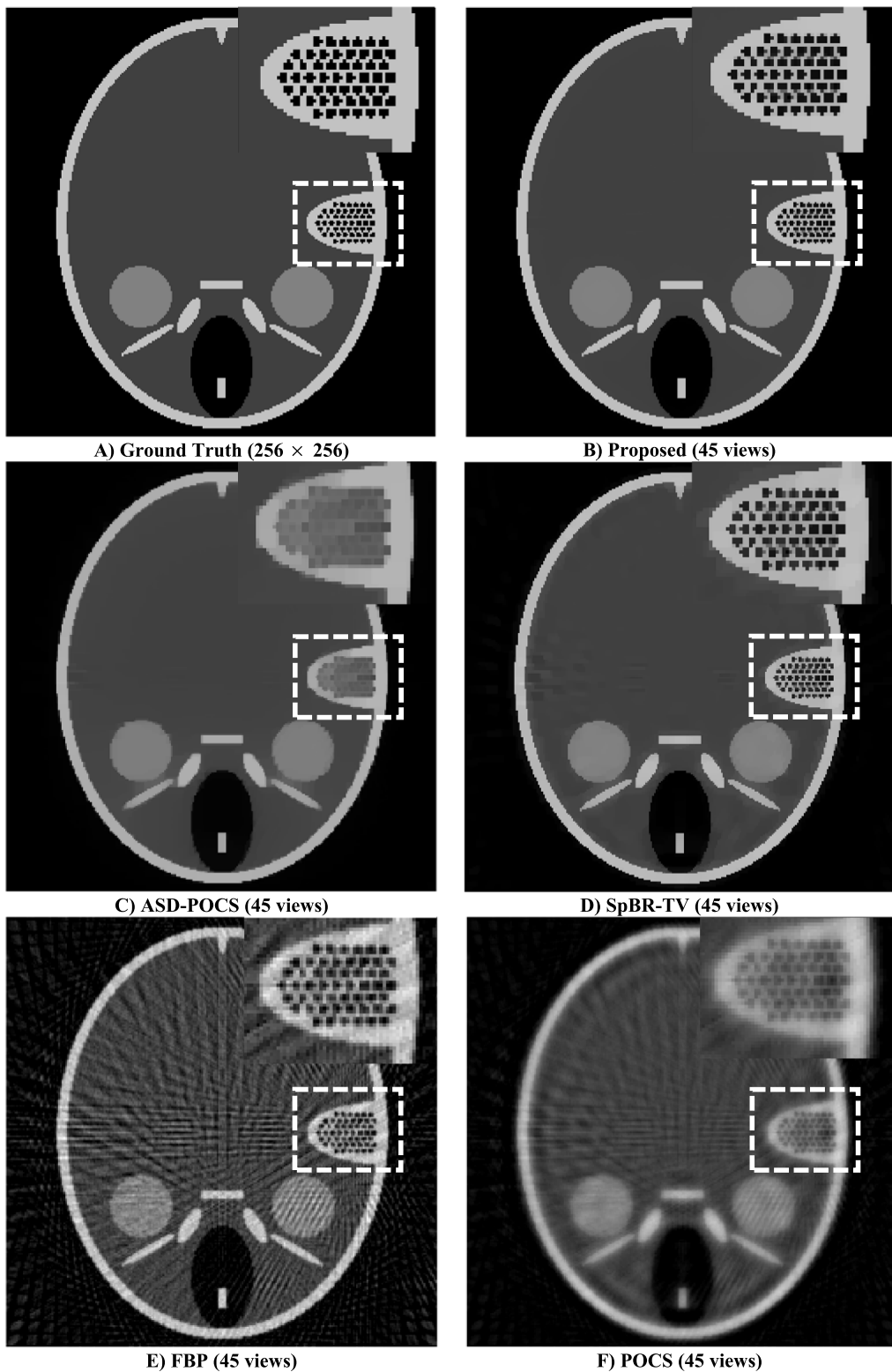


FIG. 3. Reconstructed synthetic FORBILD head phantom Images using 45 views.

FORBILD head phantom and a single transverse slice of a femoral cortical bone. In both the cases, the reconstruction algorithms were implemented at different numbers of projections that were uniformly sampled from the full projection dataset. MATLAB R2014b software was used to implement the algorithms on a desktop PC with six Intel® Xeon® CPU 2 GHz processors and 32 GB memory.

A. Simulation—Reconstructed images of a synthetic head phantom

A synthetic FORBILD head phantom⁵⁰ was used as the ground truth image in the first experiment because it has features with different sizes. The size of this phantom image is 256×256 pixels. Five images were reconstructed by the FBP,

TABLE II. Quality metrics of the reconstructed femoral cortical bone image.

| Number of projections method | 90 | | | 180 | | | 270 | | |
|------------------------------|--------|-----------|--------|--------|-----------|--------|--------|-----------|--------|
| | SSIM | PSNR (dB) | RE (%) | SSIM | PSNR (dB) | RE (%) | SSIM | PSNR (dB) | RE (%) |
| Proposed | 0.6595 | 29.29 | 18.77 | 0.6739 | 30.74 | 14.69 | 0.7160 | 32.45 | 12.28 |
| SpBR-TV | 0.6119 | 27.91 | 21.99 | 0.6522 | 29.56 | 16.83 | 0.6929 | 31.32 | 13.99 |
| ASD-POCS | 0.5537 | 26.03 | 27.29 | 0.6346 | 28.67 | 18.64 | 0.6886 | 30.35 | 15.64 |
| POCS | 0.4979 | 24.76 | 31.6 | 0.5276 | 26.53 | 23.85 | 0.6006 | 28.79 | 18.71 |
| FBP | 0.1386 | 18.36 | 66.02 | 0.2533 | 22.11 | 39.67 | 0.3700 | 25.27 | 28.06 |

POCS, ASD-POCS, and SpBR-TV methods and the proposed algorithm using 15, 25, 45, and 90 projections. Table I shows the quality assessment metrics of the reconstructed images with different numbers of projections. The proposed algorithm has the highest PSNR, SSIM, and lowest RE with respect to other methods even when the number of projections is only 15. The difference in results between the proposed algorithm and the other methods is from the fact that FORBILD head phantom is uniform within organs and has a limited number of abrupt variations at the organ boundaries. This structure completely corresponds with the prior assumption in the proposed algorithm, i.e., gradient domain sparseness. To better illustrate the effectiveness of the proposed algorithm, the quality metrics were plotted individually in Fig. 2. In addition, a visual comparison of the reference image with the other reconstructed images using 45 projections was shown in Fig. 3. As shown in Fig. 3(e), the aliasing artifact generated by incomplete projected data is obviously apparent in the image reconstructed by the FBP method. Although the aliasing artifact is somewhat suppressed in the image reconstructed by the POCS method (Fig. 3(f)), the blurring artifact is generated which reduced the image spatial resolution. The ASD-POCS method recovers smooth (low spatial frequency) regions and reduces or completely removes aliasing artifacts in these areas but as shown in the enlarged area (Fig. 3(c)), the small (high spatial frequency) structures are over-smoothed. The image

reconstructed by the SpBR-TV method in Fig. 3(d) shows that the method is successful in preserving prominent edges and at the same time suppressing the aliasing artifact without the generation of the blurring artifact or over-smoothed image. However, this method suffers from staircase effect. On the other hand, as shown in Fig. 3(b), the proposed algorithm suppresses the aliasing artifact and simultaneously almost preserves all image features. The enlarged image areas are shown in Fig. 3 to better visualize the quality of the reconstructed images. According to the result shown, we can conclude that the proposed algorithm is more successful in forming artifact suppression–spatial resolution trade-off than the other methods.

B. Real data—Reconstructed images of a femoral cortical bone

The proposed algorithm was used to reconstruct a single 2D slice of a block of femoral cortical bone. A reference image with the size of 2791 × 2791 pixels was reconstructed by the FBP method using the full sinogram dataset derived from all 1800 equally spaced projections spanning 180°. Five images were reconstructed by FBP, POCS, ASD-POCS, SpBR-TV, and the proposed algorithm using three different collections of undersampled sinogram data, i.e., 5% (90 views), 10% (180 views), and 15% (270 views) that were uniformly

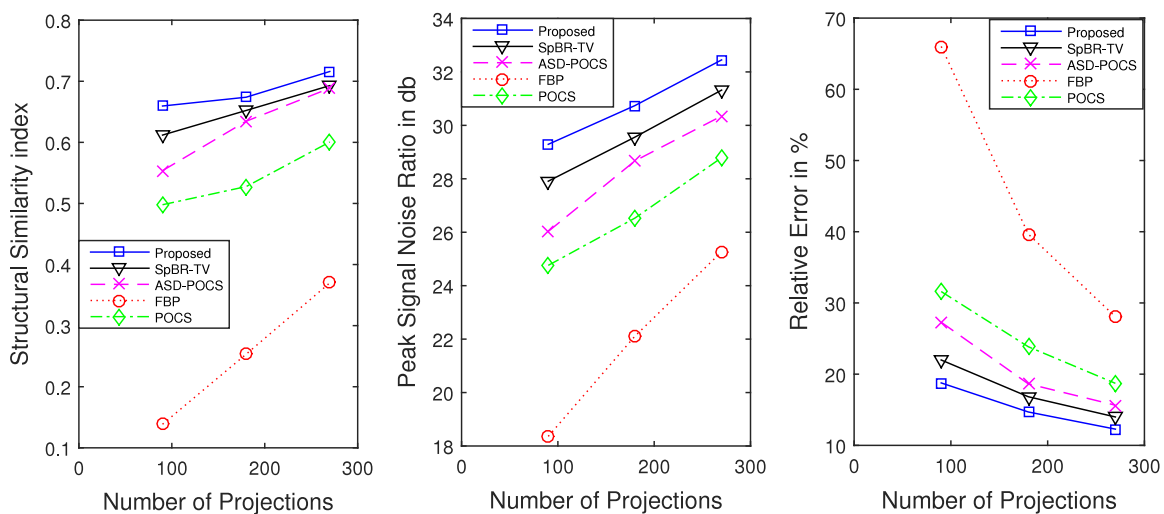


FIG. 4. Femoral cortical bone image quality metrics vs number of projections.

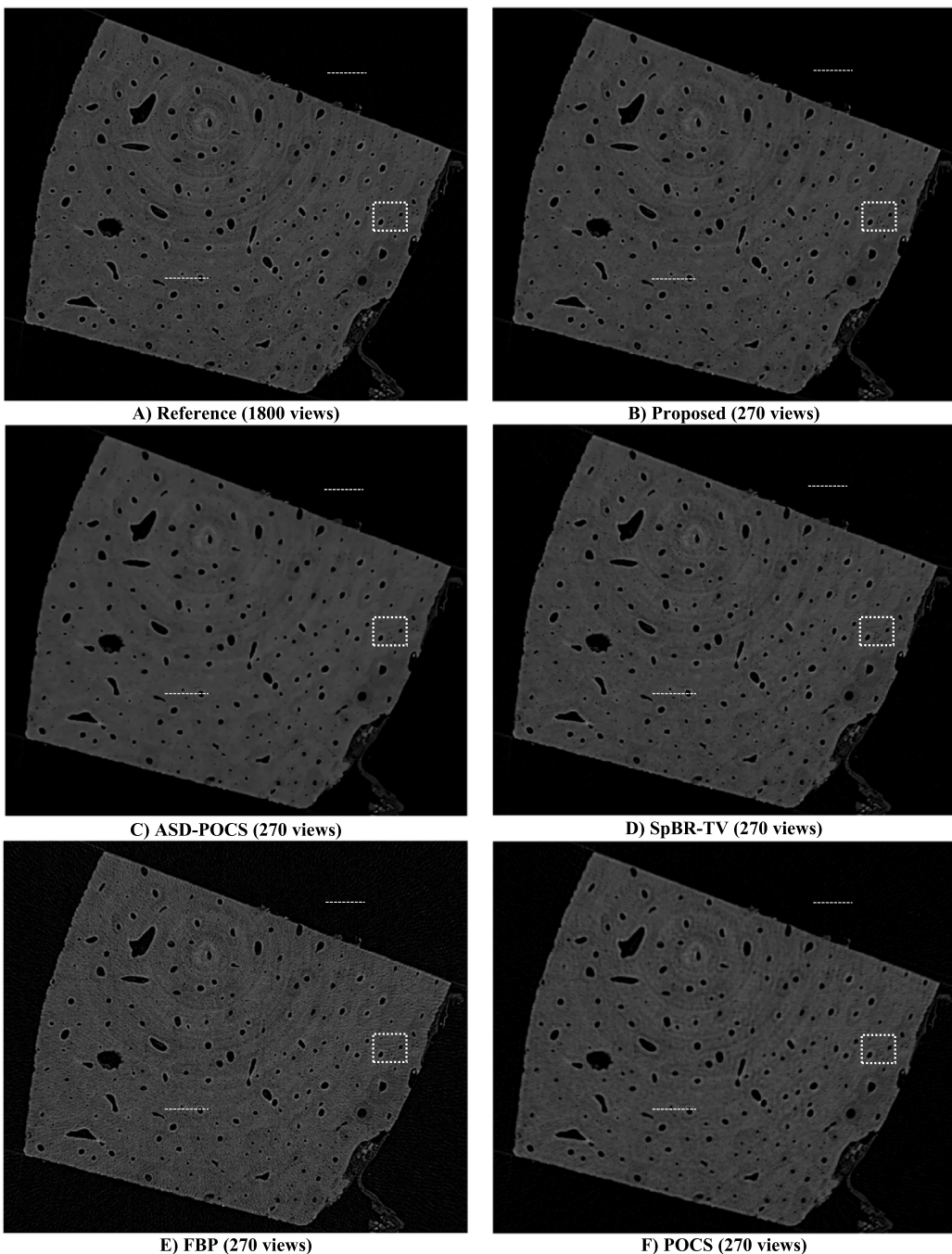


FIG. 5. The femoral cortical bone reconstructed by the different algorithms using 15% of full projection dataset (270 views). The regions of interest (the white dotted boxes) were selected to better demonstrate the details (Fig. 6), and two line profiles (the white dotted lines) in bone and surrounding air were selected to show the feature (Fig. 8) and noise (Fig. 7) profiles, respectively.

sampled from the full projection dataset. The features of interest in these bone sections are holes (vascular canals) with different sizes.

The images reconstructed by the FBP method in Figs. 5(e) and 6(e) and the line profiles in Figs. 7 and 8(a) show a pervasive aliasing artifact which is created because of insufficient numbers of projection. Therefore, the image quality is considerably reduced and there is a high chance that false features that are created by this severe artifact are incorrectly identified as true holes. The image reconstructed by the POCS method in Figs. 5(f) and 6(f) and the line profiles in Figs. 7 and 8(b) show

that the aliasing artifact is decreased, but the blurring artifact that is created by this method reduces the spatial resolution. Thus, image details such as small holes that are visible in the FBP reconstructed image have been hidden by the blurring artifact. However, as illustrated in Table II and Fig. 4, the POCS method is far superior to the FBP method in terms of existing quality metrics especially at highly incomplete projected data. The ASD-POCS method applies total-variation operator to preserve sharp edges and simultaneously remove aliasing artifacts without the generation of undesirable effects. As illustrated in Figs. 5(c) and 6(c) and the line profiles in Figs. 7 and

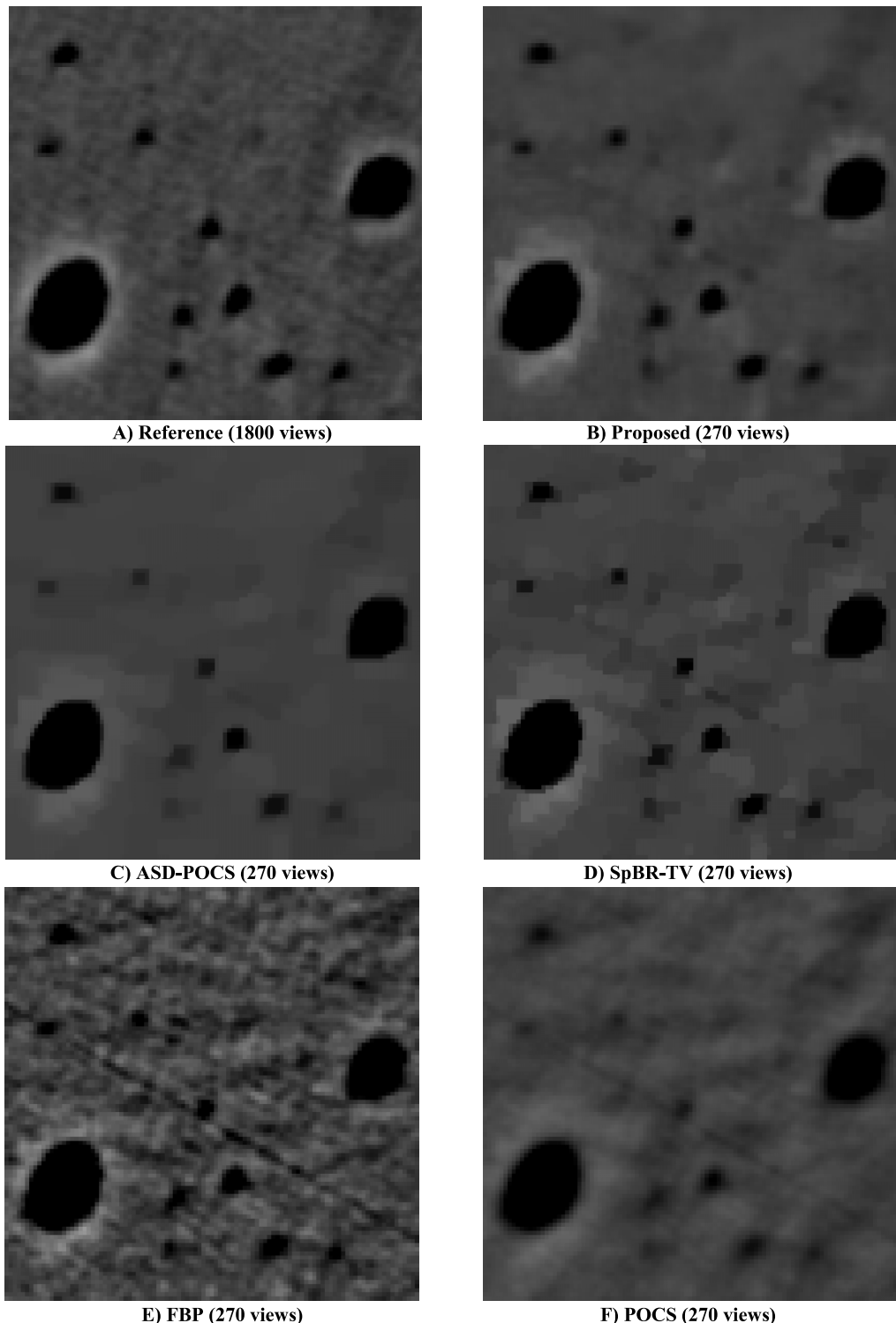


FIG. 6. The zoomed regions (the white dotted boxes in Fig. 5) in the femoral cortical bone reconstructed by the different algorithms using 15% of full projection data (270 views). The features of interest are holes (vascular canals) with different sizes.

8(c), although, this method is successful in the suppression of the aliasing artifact in the smooth regions (low-resolution features), the small structures (high-resolution features) of the image such as small holes are over-smoothed which reduces the spatial resolution. The image reconstructed by the SpBR-TV method in Figs. 5(d) and 6(d) and the line profiles in Figs. 7 and 8(d) show that the method is successful in preserving

prominent edges and at the same time suppressing the aliasing artifact without the generation of the blurring artifact or over-smoothed image. However, this method leads to the pervasive staircase effect which manifests itself as a perceptually annoying artifact. Finally, as demonstrated in Figs. 5(b) and 6(b) and the line profiles in Figs. 7 and 8, the proposed algorithm is the most successful method in controlling the trade-off between

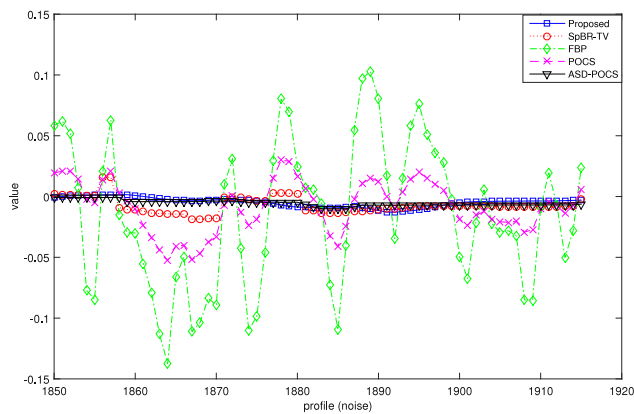


FIG. 7. Noise profiles (the white dotted lines in Fig. 5) in the air that surrounds the femoral cortical bone reconstructed by the different algorithms using 15% of full projection data (270 views).

aliasing artifact suppression and keeping spatial resolution. As shown in the zoomed area in Fig. 6, the proposed algorithm reconstructed almost all the holes which are present in the reference image while suppressing the aliasing artifact without the generation of any annoying distortion. As shown in Table II and Fig. 4, the proposed algorithm has the highest PSNR and SSIM and lowest RE with respect to the other methods even when the number of projections is only 90. From the SSIM values, one can conclude that the proposed algorithm is the best algorithm in suppressing aliasing artifacts, and the PSNR and RE values indicate that the highest reconstruction accuracy can be achieved using the proposed algorithm. Moreover, Fig. 7 shows that the noise profiles (white dotted line in the surrounding air shown in Fig. 5) of the proposed algorithm and ASD-POCS method are closer to the linear attenuation coefficient of air which is zero than the other methods noise profiles. Also, Fig. 8 shows that the feature profile (white dotted line in the bone section shown in Fig. 5) of the proposed algorithm is the closest profile to the reference image feature profile.

As shown in Fig. 6, the vascular canal (black holes) boundaries (relatively sharp contour edges) inside the rather uniform bone background which are the features of interest were accurately recovered. However, the image reconstructed by the proposed algorithm shown in Fig. 6(b) suffers from loss of structures with low contrast boundaries. To resolve this problem, the number of projections should be increased and/or the properties of the sparse regularization should be matched with the characteristics of specific samples, i.e., specific structures.

C. Parameter selection

The proposed algorithm will be successful in controlling the trade-off between artifact-suppression and spatial resolution, if the parameter λ is set to a proper value. If λ is selected too low, the problem remains inconsistent, and if it is selected too high, the final image will be over smoothed. Based on our experience, the lowest reconstruction error for our datasets was obtained when approximately $\lambda = 0.1\lambda_{\max}$ where λ_{\max} is the critical value above which the solution of the problem is

$u = 0$. The values of λ for bone data were chosen to be 0.1, 0.075, and 0.033 for 90-, 180-, and 270-view, respectively. Also, the values of λ for synthetic phantom data were chosen to be 0.021, 0.019, 0.016, and 0.012 for 15-, 25-, 45-, and 90-view, respectively.

The regularization parameter in SpBR-TV method was empirically chosen to ensure the lowest reconstruction error. The values of this parameter for bone data were chosen to be 6, 8, and 17 for 90-, 180-, and 270-view, respectively. Also, these values for synthetic phantom data were chosen to be 22, 27, 30, and 42 for 15-, 25-, 45-, and 90-view, respectively. For any regularization parameter used in the SpBR-TV method, there is a corresponding ε which was used in the ASD-POCS method to ensure fair comparison between algorithms.^{51,52} For the ASD-POCS method, the values of ε per ray measurement for bone data were chosen to be 5.25×10^{-4} , 2.18×10^{-4} , and 8.49×10^{-5} for 90-, 180-, and 270-view, respectively. Also, the values of ε per ray measurement for synthetic phantom data were chosen to be 1.40×10^{-3} , 9.05×10^{-4} , 4.47×10^{-4} and 1.06×10^{-4} for 15-, 25-, 45-, and 90-view, respectively.

D. Convergence curve

The objective function of the unconstrained problem (4) and the objective function of the SpBR-TV method²² along with the number of iterations for the bone dataset (270 projections) were plotted in Fig. 9. It shows that the proposed algorithm is faster than SpBR-TV method to converge to the practically acceptable accuracy that is needed for the kinds of real large-scale practical problems we consider. The value of the penalty parameter μ can change the path taken in getting to the final reconstructed image, so it is involved in determining the convergence speed. Based on our experience, the initial value of this parameter was set to $\mu = 0.1\lambda^{-1}$ and then we used a varying penalty parameter scheme discussed in Ref. 53 to increase the convergence speed and making the performance less dependent on the initial value. The convergence speed is also affected by the number of linear CG method iterations. We suggest to select it as small as possible, e.g., less than 10.

The proposed algorithm reconstruction time is directly proportional to the number of projections. The absolute run time of the wavelet denoising algorithm for a 270-projection bone dataset is 1 min which can be ignored because the total absolute run time of the proposed algorithm for this dataset is approximately 75 min. The reconstruction times of the proposed and competitive algorithms for the bone slice with 270 views are shown in Table III. The reconstruction time of the proposed algorithm is almost 1200 times longer than the traditional FBP method reconstruction time. However, the proposed algorithm reconstruction time is less than the other iterative algorithm's reconstruction time. As shown in Table III, the proposed algorithm needs fewer number of iterations than SpBR-TV to converge. Thus, the total reconstruction time of the proposed algorithm is less than the total reconstruction time of the SpBR-TV method. Each algorithm was run until the stopping criteria, i.e., a relative small change in the final image was met ($\varepsilon = 10^{-4}$).

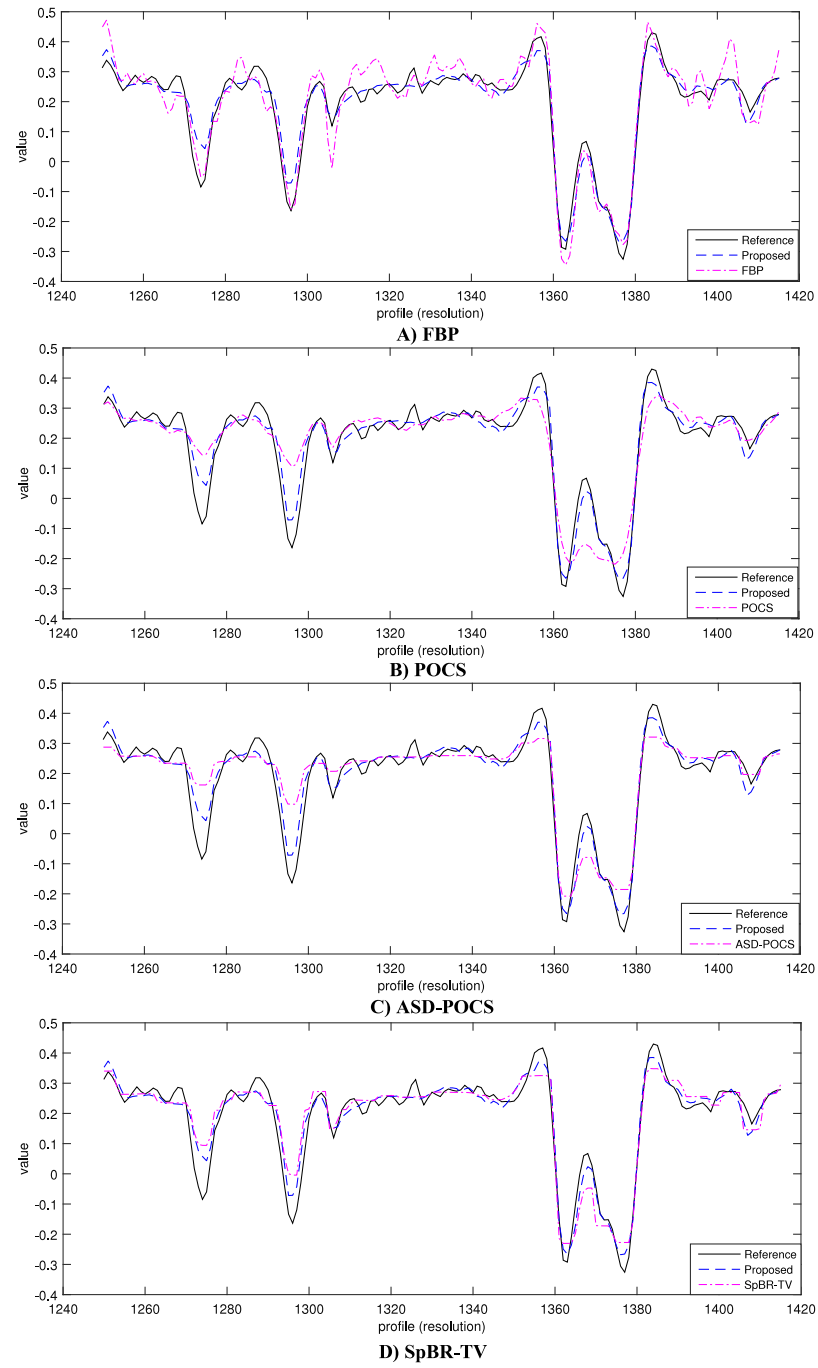


FIG. 8. Feature profiles (the white dotted lines in Fig. 5) in the femoral cortical bone reconstructed by the different algorithms using 15% of full projection data (270 views).

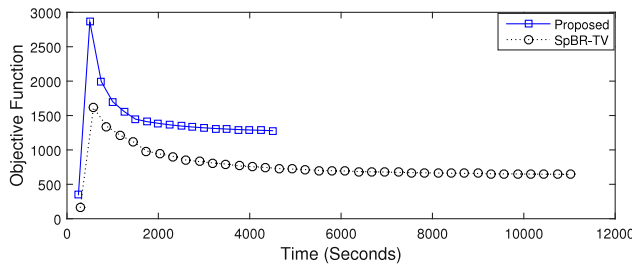


FIG. 9. Convergence curve of the proposed and SpBR-TV algorithms for bone slice with 270 views. (For better comparison, SpBR-TV objective function was multiplied by 1.5×10^{-2}).

TABLE III. Reconstruction time of the proposed and other reconstruction algorithms for a bone slice with 270 views.

| | ASD-POCS | POCS | SpBR-TV | Proposed algorithm | FBP |
|-------------------------------|----------|--------|---------|--------------------|------|
| Total reconstruction time (s) | 15 435 | 13 780 | 11 020 | 4 560 | 3.75 |
| Iteration time (s) | 735 | 530 | 290 | 250 | ... |

IV. CONCLUSIONS

In this article, we have developed and investigated a compressed sensing based reconstruction algorithm which aims to reconstruct high-quality images from synchrotron Micro-CT datasets with potential for a significant reduction in the number of projections. The proposed algorithm which is a combination of gradient-based Douglas-Rachford splitting and discrete wavelet packet shrinkage image denoising was applied to Micro-CT dataset collected in the Biomedical Imaging and Therapy bending magnet beamline at the Canadian Light Source. The algorithm solved a large-scale compressed sensing based optimization problem to achieve an optimal balance between artifact suppression and spatial resolution. Visual and quantitative performance assessment metrics were used to show the potential advantage of the proposed algorithm to the other existing reconstruction algorithms. The results illustrated that radiation dose and scan time were reduced without reduction of image quality which is an important step towards improving *in vivo* imaging protocols.

ACKNOWLEDGMENTS

The research was conducted at the Multimedia Processing and Prototyping Lab in the Department of Electrical and Computer Engineering at the University of Saskatchewan, which is funded by the Natural Sciences and Engineering Research Council of Canada (NSERC), Canada Foundation for Innovation (CFI), and Western Economic Diversification Canada. David M. L. Cooper is supported by an NSERC Discovery Grant and the Canada Research Chairs program.

- ¹G. N. Hounsfield, "Computerized transverse axial scanning (tomography): Part 1. Description of system," *Br. J. Radiol.* **46**(552), 1016–1022 (1973).
- ²L. A. Feldkamp, S. A. Goldstein, M. A. Parfitt, G. Jesion, and M. Kleerekoper, "The direct examination of three-dimensional bone architecture *in vitro* by computed tomography," *J. Bone Miner. Res.* **4**(1), 3–11 (1989).
- ³L. Grodzins, "Critical absorption tomography of small samples: Proposed applications of synchrotron radiation to computerized tomography II," *Nucl. Instrum. Methods Phys. Res., Sect. A* **206**(3), 547–552 (1983).
- ⁴P. Spanne and M. L. Rivers, "Computerized microtomography using synchrotron radiation from the NSLS," *Nucl. Instrum. Methods Phys. Res., Sect. B* **24**, 1063–1067 (1987).
- ⁵K. Sakamoto, Y. Suzuki, T. Hirano, and K. Usami, "Improvement of spatial resolution of monochromatic X-ray CT using synchrotron radiation," *Jpn. J. Appl. Phys., Part 1* **27**(1R), 127 (1988).
- ⁶B. F. McEwen, K. H. Downing, and R. M. Glaeser, "The relevance of dose-fractionation in tomography of radiation-sensitive specimens," *Ultramicroscopy* **60**(3), 357–373 (1995).
- ⁷T. Wysokinski, D. Chapman, G. Adams, M. Renier, P. Suortti, and W. Thominson, "Beamlines of the biomedical imaging and therapy facility at the Canadian light source—Part 1," *Nucl. Instrum. Methods Phys. Res., Sect. A* **582**(1), 73–76 (2007).
- ⁸J. Hsieh, *Computed Tomography: Principles, Design, Artifacts, and Recent Advances* (SPIE, Bellingham, WA, 2009).
- ⁹J. F. Barrett and N. Keat, "Artifacts in CT: Recognition and avoidance 1," *Radiographics* **24**(6), 1679–1691 (2004).
- ¹⁰R. Gordon, R. Bender, and G. T. Herman, "Algebraic reconstruction techniques (ART) for three-dimensional electron microscopy and X-ray photography," *J. Theor. Biol.* **29**(3), 471–481 (1970).
- ¹¹C. K. Avinash and M. Slaney, *Principles of Computerized Tomographic Imaging* (IEEE Press, 1988).
- ¹²M. Beister, D. Kolditz, and W. A. Kalender, "Iterative reconstruction methods in X-ray CT," *Physica Med.* **28**(2), 94–108 (2012).
- ¹³J. S. Jørgensen, E. Y. Sidky, P. C. Hansen, and X. Pan, "Empirical average-case relation between undersampling and sparsity in x-ray CT," *Inverse Probl. Imaging* **9**(2), 431 (2015).
- ¹⁴J. S. Jørgensen, C. Kruschel, and D. A. Lorenz, "Testable uniqueness conditions for empirical assessment of undersampling levels in total variation-regularized X-ray CT," *Inverse Probl. Sci. Eng.* **23**(8), 1283–1305 (2015).
- ¹⁵E. Y. Sidky, C. M. Kao, and X. Pan, "Accurate image reconstruction from few-views and limited-angle data in divergent-beam CT," *J. X-Ray Sci. Technol.* **14**(2), 119–139 (2006).
- ¹⁶E. Y. Sidky and X. Pan, "Image reconstruction in circular cone-beam computed tomography by constrained, total-variation minimization," *Phys. Med. Biol.* **53**(17), 4777 (2008).
- ¹⁷X. Han, J. Bian, D. R. Eaker, T. L. Kline, E. Y. Sidky, E. L. Ritman, and X. Pan, "Algorithm-enabled low-dose micro-CT imaging," *IEEE Trans. Med. Imaging* **30**(3), 606–620 (2011).
- ¹⁸C. G. Graff and E. Y. Sidky, "Compressive sensing in medical imaging," *Appl. Opt.* **54**(8), 23–44 (2015).
- ¹⁹S. Ramani and J. A. Fessler, "An accelerated iterative reweighted least squares algorithm for compressed sensing MRI," in *IEEE International Symposium on Biomedical Imaging: From Nano to Macro* (IEEE, 2010), pp. 257–260.
- ²⁰A. Beck and M. Teboulle, "A fast iterative shrinkage-thresholding algorithm for linear inverse problems," *SIAM J. Imaging Sci.* **2**(1), 183–202 (2009).
- ²¹A. Beck and M. Teboulle, "Fast gradient-based algorithms for constrained total variation image denoising and deblurring problems," *IEEE Trans. Image Process.* **18**(11), 2419–2434 (2009).
- ²²T. Goldstein and S. Osher, "The split Bregman method for L1-regularized problems," *SIAM J. Imaging Sci.* **2**(2), 323–343 (2009).
- ²³S. Ramani and J. A. Fessler, "A splitting-based iterative algorithm for accelerated statistical X-ray CT reconstruction," *IEEE Trans. Med. Imaging* **31**(3), 677–688 (2012).
- ²⁴A. Chambolle and T. Pock, "A first-order primal-dual algorithm for convex problems with applications to imaging," *J. Math. Imaging Vision* **40**(1), 120–145 (2011).
- ²⁵E. Y. Sidky, H. J. Jakob, and X. Pan, "Convex optimization problem prototyping for image reconstruction in computed tomography with the Chambolle-Pock algorithm," *Phys. Med. Biol.* **57**(10), 3065 (2012).
- ²⁶E. Esser, X. Zhang, and T. F. Chan, "A general framework for a class of first order primal-dual algorithms for convex optimization in imaging science," *SIAM J. Imaging Sci.* **3**(4), 1015–1046 (2010).
- ²⁷B. Vandeginste, B. Goossens, J. D. Beenhouwer, A. Pizurica, W. Philips, S. Vandenbergh, and S. Staelens, "Split-Bregman-based sparse-view CT reconstruction," in *11th International Meeting on Fully Three-Dimensional Image Reconstruction in Radiology and Nuclear Medicine*, Potsdam, Germany, 2011, pp. 431–434.
- ²⁸L. Ritschl, F. Bergner, C. Fleischmann, and M. Kachelrieß, "Improved total variation-based CT image reconstruction applied to clinical data," *Phys. Med. Biol.* **56**(6), 1545 (2011).
- ²⁹J. Song, Q. H. Liu, G. A. Johnson, and C. T. Badea, "Sparseness prior based iterative image reconstruction for retrospectively gated cardiac micro-CT," *Med. Phys.* **34**(11), 4476–4483 (2007).
- ³⁰J. Douglas and H. H. Rachford, "On the numerical solution of heat conduction problems in two and three space variables," *Trans. Am. Math. Soc.* **82**(2), 421–439 (1956).
- ³¹D. L. Donoho, I. M. Johnstone, G. Kerkyacharian, and D. Picard, "Wavelet shrinkage: Asymptopia?," *J. R. Stat. Soc. Ser. B (Methodological)* **57**(2), 301–369 (1995); available at <http://www.jstor.org/stable/2345967>.
- ³²J. Zhong, R. Ning, and D. Conover, "Image denoising based on multiscale singularity detection for cone beam CT breast imaging," *IEEE Trans. Med. Imaging* **23**(6), 696–703 (2004).
- ³³A. Fathi and A. R. Naghsh-Nilchi, "Efficient image denoising method based on a new adaptive wavelet packet thresholding function," *IEEE Trans. Image Process.* **21**(9), 3981–3990 (2012).
- ³⁴B. Wolkowski, E. Snead, M. Wesolowski, J. Singh, M. Pettitt, R. Chibbar, S. A. Melli, and J. Montgomery, "Assessment of freeware programs for the reconstruction of tomography datasets obtained with a monochromatic synchrotron-based X-ray source," *J. Synchrotron Radiat.* **22**(4), 1130–1138 (2015).
- ³⁵E. Walters, W. Simon, D. A. Chesler, and J. A. Correia, "Attenuation correction in gamma emission computed tomography," *J. Comput. Assisted Tomogr.* **5**, 89–94 (1981).
- ³⁶X. L. Xu, J. S. Liaw, and S. C. Strother, "Iterative algebraic reconstruction algorithms for emission computed tomography," *Med. Phys.* **20**, 1675–1684 (1993).

- ³⁷G. L. Zeng and G. T. Gullberg, "Unmatched projector/backprojector pairs in an iterative reconstruction algorithm," *IEEE Trans. Med. Imaging* **19**(5), 548–555 (2000).
- ³⁸C. L. Epstein, *Introduction to the Mathematics of Medical Imaging* (Prentice Hall, Upper Saddle River, NJ, 2003).
- ³⁹D. S. Lalush and B. M. W. Tsui, "Improving the convergence of iterative filtered backprojection algorithm," *Med. Phys.* **21**, 1283–1286 (1994).
- ⁴⁰S. S. Chen, D. L. Donoho, and M. A. Saunders, "Atomic decomposition by basis pursuit," *SIAM Rev.* **43**(1), 129–159 (2001).
- ⁴¹R. Tibshirani, "Regression shrinkage and selection via the lasso," *J. R. Stat. Soc.: Ser. B (Methodological)* **58**(1), 267–288 (1996); available at <http://www.jstor.org/stable/2346178>.
- ⁴²D. P. Bertsekas, *Constrained Optimization and Lagrange Multiplier Methods* (Academic Press, 2014).
- ⁴³J. Eckstein and D. P. Bertsekas, "On the Douglas—Rachford splitting method and the proximal point algorithm for maximal monotone operators," *Math. Program.* **55**(1-3), 293–318 (1992).
- ⁴⁴N. Parikh and S. P. Boyd, "Proximal algorithms," *Found. Trends Optim.* **1**(3), 127–239 (2014).
- ⁴⁵M. R. Hestenes and E. Stiefel, "Methods of conjugate gradients for solving linear Systems," *J. Res. Natl. Bur. Stand.* **49**, 409 (1952).
- ⁴⁶M. Lustig, D. Donoho, and J. M. Pauly, "Sparse MRI: The application of compressed sensing for rapid MR imaging," *Magn. Reson. Med.* **58**(6), 1182–1195 (2007).
- ⁴⁷A. M. Alotaibi and M. T. Ismail, "A comparison of some thresholding selection methods for wavelet regression," *World Acad. Sci. Eng. Technol.* **62**(1), 119–125 (2010).
- ⁴⁸S. Boyd, N. Parikh, E. Chu, B. Peleato, and J. Eckstein, "Distributed optimization and statistical learning via the alternating direction method of multipliers," *Found. Trends Mach. Learn.* **3**(1), 1–122 (2011).
- ⁴⁹Z. Wang, A. C. Bovik, H. R. Sheikh, and E. P. Simoncelli, "Image quality assessment: From error visibility to structural similarity," *IEEE Trans. Image Process.* **13**(4), 600–612 (2004).
- ⁵⁰See <http://www.imp.uni-erlangen.de/phantoms> for more information about FORBILD head phantom.
- ⁵¹R. T. Rockafellar, *Convex Analysis* (Princeton University Press, 2015).
- ⁵²J. Bian, J. H. Siewersden, X. Han, E. Y. Sidky, J. L. Prince, C. A. Pelizzari, and X. Pan, "Evaluation of sparse-view reconstruction from flat-panel-detector cone-beam CT," *Phys. Med. Biol.* **55**(22), 6575 (2010).
- ⁵³S. L. Wang and L. Z. Liao, "Decomposition method with a variable parameter for a class of monotone variational inequality problems," *J. Optim. Theory Appl.* **109**(2), 415–429 (2001).